buildings

MDPI

Article

Cyclic Behavior of Joints Assembled Using Prefabricated Beams and Columns with High-Ductility Recycled Powder Concrete

Xiuling Li [1,2,*], Haodong Sun [2], Kezhen Chen [2], Tianfeng Yuan [2], Long Wen [2], Xiaowei Zheng [3] and Tongxing Bu [2]

[1] School of Civil Engineering, Shandong Jiaotong University, Jinan 250357, China
[2] Key Laboratory of Building Structural Retrofitting and Underground Space Engineering, Shandong Jianzhu University, Ministry of Education, Jinan 250101, China; horizonsun77@163.com (H.S.)
[3] School of Mechanics and Civil Engineering, China University of Mining and Technology, Xuzhou 221116, China
* Correspondence: dlutiem@163.com

Abstract: The integration of recycled powder (RP) as a partial cement replacement in concrete, combined with fiber reinforcement, facilitates the development of high-ductility recycled powder concrete (HDRPC) with enhanced mechanical properties. This approach holds significant potential for effectively recycling construction waste and reducing carbon emissions. To improve the seismic performance of prefabricated joints in industrial prefabricated building production, experimental tests under low-cycle reversed cyclic loading were conducted on four HDRPC prefabricated joints, one HDRPC cast-in-place joint, and one normal prefabricated concrete joint. The study systematically analyzed damage patterns, deformation ductility, stiffness degradation, hysteresis energy dissipation, and other performance characteristics. The results demonstrate that HDRPC effectively mitigates crack width and shear deformation in the joint core area, achieving a 17.8% increase in joint-bearing capacity and a 33.3% improvement in displacement ductility. Moreover, HDRPC improves specimen damage characteristics, enhances joint shear capacity and flexibility, and reduces the demand for hoop reinforcement in the joint core area due to its exceptional shear ductility. Based on the softened tension–compression bar model, a crack-resistance-bearing capacity equation for HDRPC joints was derived, which aligns closely with shear test results when cracks develop in the joint core area.

Keywords: high-ductility recycled powder concrete; prefabricated beam–column joints; cyclic behavior; hysteresis curve; joint shear capacity

check for updates

Academic Editor: Ciro Del Vecchio

Received: 10 February 2025
Revised: 3 March 2025
Accepted: 4 March 2025
Published: 6 March 2025

Citation: Li, X.; Sun, H.; Chen, K.; Yuan, T.; Wen, L.; Zheng, X.; Bu, T. Cyclic Behavior of Joints Assembled Using Prefabricated Beams and Columns with High-Ductility Recycled Powder Concrete. *Buildings* **2025**, *15*, 838. https://doi.org/10.3390/buildings15050838

Copyright: © 2025 by the authors. Licensee MDPI, Basel, Switzerland. This article is an open access article distributed under the terms and conditions of the Creative Commons Attribution (CC BY) license (https://creativecommons.org/licenses/by/4.0/).

1. Introduction

The construction industry significantly impacts global sustainability due to inefficient resource utilization, environmental degradation, and reliance on traditional production methods. Notably, construction activities account for approximately 40% of global energy consumption and 36% of carbon emissions [1,2]. As a major contributor to climate change, the industry faces growing pressure to adopt low-carbon, eco-friendly solutions [3]. Among these, prefabricated structures and recycled concrete have emerged as promising alternatives, leveraging construction and demolition waste to mitigate environmental impacts and conserve resources [4,5].

Prefabricated structures, while offering advantages in construction efficiency and sustainability, often exhibit weak characteristics under seismic loading. Previous studies

have identified several critical issues, including brittle failure at beam–column joints, inadequate energy-dissipation capacity, and limited ductility due to insufficient reinforcement detailing and poor connection integrity [6,7]. For instance, post-earthquake investigations of precast reinforced concrete structures have revealed that joint failures are a common cause of structural collapse, particularly in regions with high seismic activity [8–10]. These findings underscore the need for improved joint designs that enhance seismic resilience while maintaining the benefits of prefabrication.

The incorporation of recycled concrete in construction materials offers significant environmental and social benefits by reducing carbon emissions and promoting efficient use of solid waste resources [11]. Notably, construction waste generates a large volume of fine particles under 150 μm, commonly referred to as recycled powder (RP), which constitutes approximately 20% of the raw material used [12,13]. Extensive research has explored the potential of RP in improving engineering cement-based composite materials. The feasibility of using recycled powder to produce high-performance concrete has been validated through studies on particle size distribution [14,15], chemical composition [16,17], fiber interactions [18–21], and empirical investigations [22].

High-ductility recycled powder concrete (HDRPC) is an eco-friendly material that offers substantial improvements over normal concrete in terms of ductility, crack resistance, and durability [23,24]. HDRPC, which typically incorporates a high replacement ratio of recycled powder and hybrid fibers such as basalt fibers (BFs) and polyvinyl alcohol (PVA) fibers, demonstrates enhanced fracture resistance and improved ductility due to better matrix–fiber interaction [25–28]. Yu et al. [29] developed a carbon-emission-calculation model for prefabricated buildings based on life cycle assessment (LCA) theory, evaluated the environmental impact of green building materials, and quantitatively calculated the carbon emissions of HDRPC during the materialization phase, showing that HDRPC has better environmental benefits than C30 concrete, with a 31.86 kgCO_2e reduction in emissions per structure. This makes HDRPC an ideal candidate for strengthening and repairing reinforced concrete (RC) structures, including beam–column joints under both static and seismic loading conditions [30]. However, while the properties of HDRPC have been explored for general concrete applications, its performance in the joint areas of prefabricated RC structures remains under-researched.

Prefabricated buildings have gained significant attention due to their efficiency, sustainability, and potential for reducing construction time and costs. Among the various components in a prefabricated structure, the beam–column joint is particularly critical in ensuring the overall performance and safety of the structure. Current connection techniques for prefabricated elements include bolting, welding, riveting, and grouting, with grouting sleeves being one of the most widely adopted methods for connecting precast components [31]. These sleeves help join prefabricated elements either horizontally [32–34] or vertically [35–38], transferring internal forces and meeting seismic design requirements. Grouting sleeves enhance the load-bearing capacity and rigidity of joints, forming a "rigid zone" that helps prevent crushing or damage under seismic loads [39]. Joints connect elements, transfer internal loads, and maintain structural integrity in assembled concrete frame structures. Important stress point affects the seismic performance of structures. The joint must be strong, stiff, and ductile for earthquake bearing and deformation [40,41]. The strength, stiffness, and ductility of joints are crucial for earthquake resistance, and several studies have focused on improving the mechanical behavior of prefabricated beam–column joints to increase their seismic performance [42–44]. Ding et al. [42] proposed a prefabricated concrete beam–column joint with a bolt connection and investigated its seismic performance through full-scale experiments and finite element simulations, with experimental results showing that joints connected by grade 8.8 bolts exhibit higher yield and

ultimate bearing capacities, initial stiffness, and energy consumption compared to those connected by grade 5.6 bolts, while simulations further explore the impact of bolt strength and axial compression ratio on the seismic behavior of the joint. Zhang et al. [43] present cyclic tests of four interior precast UHPC (ultra-high-performance concrete)/RC composite beam–column joints to evaluate the impact of replacing normal concrete with UHPC in the joint zone, showing that non-steam-cured UHPC exhibits high compressive and tensile strength, eliminates the need for stirrups, and allows for significantly reduced anchorage lengths, thus simplifying the fabrication process. Several approaches [45–47] have been proposed to increase load-bearing, ductility, and energy dissipation of prefabricated frame beam–column connections. Huang et al. [45] propose a novel dry precast concrete beam–column connection with multi-slit devices (MSDs) and investigate its seismic performance through cyclic loading tests on three full-scale specimens, showing that the precast joints outperform cast-in-place joints in terms of load-carrying capacity, stiffness, energy dissipation, and deformation capacity, making them suitable for high-risk earthquake regions. Ye et al. [46] propose a new fully precast replaceable energy-dissipation rocking beam–column joint (RBCJ) with energy-dissipating steel plates, and investigate its seismic performance through quasi-static tests on two scaled specimens, demonstrating that the joint has small residual displacement, concentrated plastic deformation in replaceable parts, and excellent repairable performance, with the short-lap specimen outperforming the long-lap one in seismic performance and recovery.

Recent research has proposed various strategies to enhance the seismic resilience of prefabricated frame joints, such as introducing new connection forms [48–51] and utilizing high-performance concretes [52–55]. Notably, some studies have examined the use of UHPC to improve the shear strength and cyclic performance of prefabricated joints [56,57]. Lin et al. [57] propose a novel precast beam–column connection with a UHPC core-shell and investigate its seismic performance through quasi-static tests on three precast and one monolithic specimen, showing that the UHPC shell effectively limits shear behavior, delays cracking, enhances ductility, and improves energy dissipation, while allowing for fewer stirrups than required by code. Similarly, high-ductility concrete (HDC) has been investigated for improving the shear-bearing capacity of prefabricated beam–column connections [58]. Deng et al. [58] investigate the use of HDC in five precast beam–column connections under cyclic loading, showing that HDC significantly improves shear and damage-tolerance capacities, shifts failure from joint shear to beam end and can replace stirrups in confining joints, though column strengthening is required to meet "strong column" criteria. Despite the advancements in prefabricated structures, there remains a significant research gap in the application of HDRPC for enhancing the seismic performance of beam–column joints. Previous studies have primarily focused on normal concrete or UHPC, with limited exploration of HDRPC in prefabricated joints.

This study seeks to address the existing gap in knowledge by evaluating the cyclic behavior of HDRPC joints under varying axial loads and stirrup configurations. The objectives of this research are as follows: (1) to investigate the seismic performance of HDRPC joints in comparison to normal concrete joints, (2) to develop design guidelines for HDRPC joints based on both experimental and theoretical analyses, and (3) to explore the potential of HDRPC in reducing the demand for hoop reinforcement, thus simplifying construction processes. The experimental results will provide valuable insights into the fracture resistance and shear-carrying capacity of HDRPC-prefabricated joints, contributing essential data for the development of design formulas. Ultimately, the findings of this study will support the advancement of prefabricated structures using HDRPC, laying a solid foundation for their application in earthquake-prone regions.

2. Materials and Mixture Proportions

2.1. Normal Concrete

To decrease the amount of cement used and enhance the efficiency of recycled powder, the non-critical stress areas of the nodal specimens in this experiment were made with normal recycled powder concrete (NRPC) [4]. Table 1 displays the two common concrete mixtures used in the PC30 joints. Table 2 shows the parameters of the regenerated powder used in the experiment. A cubic compressive strength test was conducted, and the amount of water-reducing agent was determined based on the ease of mixing. The results of the test can be found in Table 3 and Figure 1. Type I normal Portland cement and the normal river sand of fine aggregate were adopted. The coarse aggregate was used crushed aggregate with a maximum size of 16 mm in diameter. The compressive strengths were tested using materials from the same batch as the beam–column joint specimens.

Table 1. Mix proportions of concrete.

Type of Concrete	RCP Replacement Percentage (%)	Water-to-Binder Ratio	Sand-to-Binder Ratio	HRWR [3] (%)	PVA Fiber [4] (vol.%)	Basalt Fiber (vol.%)
C30	-	0.41	0.42	0.21	-	-
C35	-	0.38	0.42	0.26	-	-
NRPC [1]	50	0.41	0.42	0.26	-	-
HDRPC [2]	45	0.32	0.40	0.17	1.7	0.2

[1] "NRPC" is normal recycled concrete; [2] "HDRPC" is high-ductility recycled powder concrete; [3] "HRWR" is a high-range water reducer used to improve the flow ability of concrete; [4] "PVA fiber" is polyvinyl alcohol fiber.

Table 2. Parameters of recycled powder.

Density ($g \cdot cm^{-3}$)	Moisture Content (%)	Heat Loss (%)	Characteristic Parameters of Particle Size (μm)		
			D10	D50	D90
2.63	2.1	25.7	0.99	4.51	16.18
Major oxides content (%)	CaO	SiO_2	Al_2O_3	MgO	Fe_2O_3	K_2O
	44.5	23.05	6.41	2.6	2.48	1.3

Table 3. Compressive strength of NRPC.

Replacement Rate (%)	Water-Reducing Agent ($kg \cdot m^{-3}$)	7 d Water Curing (MPa)	28 d Water Curing (MPa)	28 d Natural Curing (MPa)
0	4.40	48.4	58.2	53.6
10	4.40	40.5	51.8	46.4
20	4.62	40.8	52.8	49.2
30	4.84	35.3	46	41.4
40	5.72	35.7	46.7	41.9
50	6.60	27.6	36.8	34.5

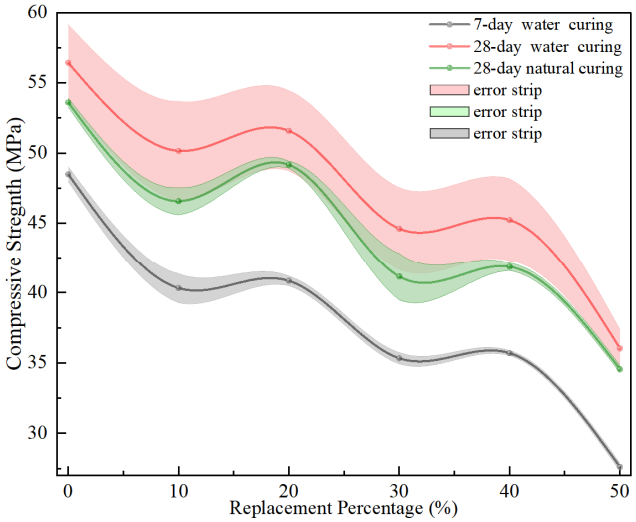


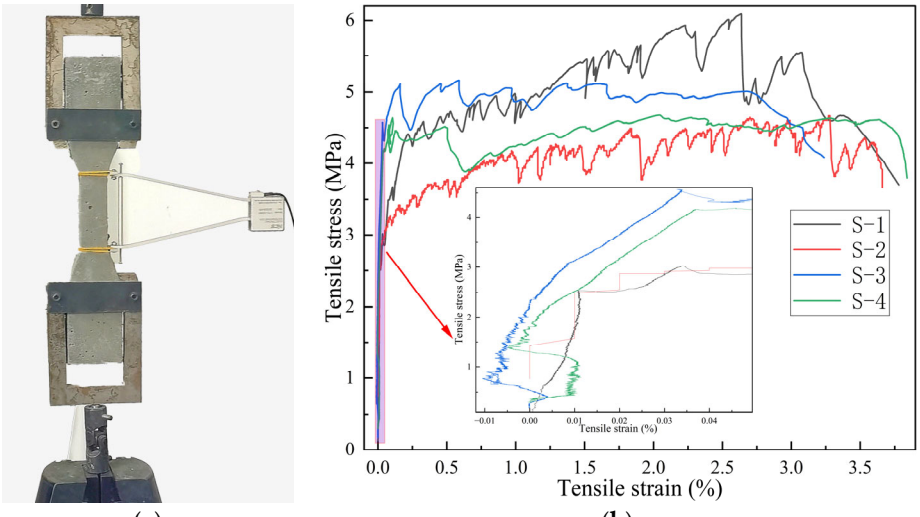
Figure 1. Compressive strength of NRPC.

2.2. High-Ductility Recycled Powder Concrete

High-ductility recycled powder concrete (HDRPC) was formulated using cement, fly ash, recycled powder, quartz sand, water, a high-range water reducer, basalt fibers (BFs), and polyvinyl alcohol (PVA) fibers. Table 4 shows the parameters of different fibers used in the experiment. Detailed mix proportions are presented in Table 1. To evaluate tensile behavior, four dog-bone-shaped specimens were tested, yielding an average tensile strength of 5.15 MPa and an ultimate strain of 3.63%, meeting the requirements for engineered cementitious composites (ECC) (Figure 2).

Table 4. Parameters of fiber.

Type of Fiber	Density (kg·m^{-3})	Tensile Strength (MPa)	Tensile Limit (%)	Length (mm)	Modulus (GPa)	Diameter (μm)
PVA	1300	1620	6.0–8.0	12	42.8	39
Basalt fiber	2650	2320	2.6	18	84.5	15

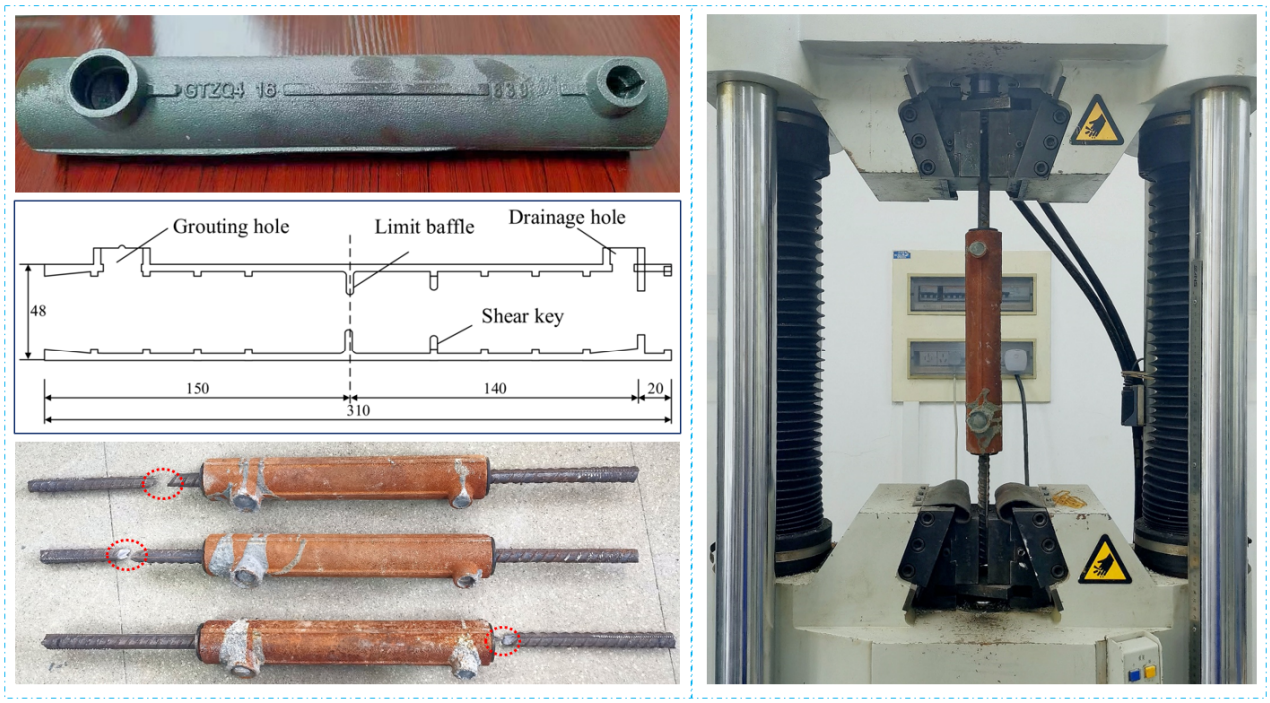


(**a**) (**b**)

Figure 2. Tensile test of the HDRPC: (**a**) specimen (unit: mm); (**b**) stress–strain curves.

2.3. Grouting Sleeves and Grouts

According to the "Technical Specification for Splicing of Reinforced Grouting Sleeves" JGJ 355-2015 [59], the selected cast iron fully grouted sleeve GTZQ4 16 (Figure 3) was tested. Three fully grouted sleeves were randomly selected for testing to verify their uniaxial tensile performance, and the test results showed that the steel bars were broken and ultimately destroyed. The test results are listed in Table 5. The results showed that the fully grouted sleeve used in this experiment met the specified requirements and achieved an efficient and reliable connection of steel bars between prefabricated beams and columns.



(**a**) (**b**)

Figure 3. Cast iron fully grouted sleeve: (**a**) grouting sleeve and failure mode; (**b**) test setup.

Table 5. Uniaxial tensile properties of grouted sleeve steel bar connections.

Connector Number	1	2	3	Regulatory Requirement
Tensile strength (MPa)	635	612	637	$\geq f_{stk}$ [1]
Total elongation (%)	12.2	11.4	12.5	≥6.0

[1] f_{stk} is the standard value of the ultimate strength of steel bars.

3. Mechanical Properties

3.1. Design of Test Specimens

To evaluate the connection behavior of the RC frame with beam and column, six full-scale specimens were prepared in this study. The beam cross-sections had dimensions of 250 mm × 300 mm, while the column cross-sections had dimensions of 300 mm × 300 mm. The precast beams and columns are joined together using grout sleeves to extend the whole depth of the joint beam contact. During seismic loading, the core area of the joint and the neighboring beam and column ends in the back-cast zone are anticipated to endure significant shear forces and bending moments. Consequently, the areas of high stress were reinforced using HDRPC material, whereas the rest of the specimen was made with NRPC. The axial load ratios (0.3, 0.5, 0.7) were selected to represent a range of axial compression conditions typically encountered in prefabricated structures. These values were chosen based on previous studies and design practices, where 0.3 simulates moderate axial loading,

while 0.5 and 0.7 represent higher axial compression scenarios, such as those found in multi-story buildings or structures subjected to significant gravity loads [60].

The reinforcement detailing and stirrup spacing were designed by the Chinese Code for Design of Concrete Structures (GB 50010-2010) [61]. Stirrup spacings of 100 mm and 200 mm were selected to evaluate the effect of hoop-reinforcement density on joint performance. A spacing of 100 mm represents a dense reinforcement configuration, while 200 mm represents a reduced reinforcement scenario, allowing us to assess whether HDRPC can compensate for reduced stirrup density. The specific characteristics of the specimen, including its specifications and construction details, are provided in Table 6 and Figure 4a–d. The compressive strength of normal concrete and HDRPC was tested at 28 days, yielding values of 38.1 MPa and 32.3 MPa, respectively, which exceed the minimum requirements of GB 50010-2010 [61]. The yield strength of the steel reinforcement was 420 MPa, consistent with the design value specified in the code.

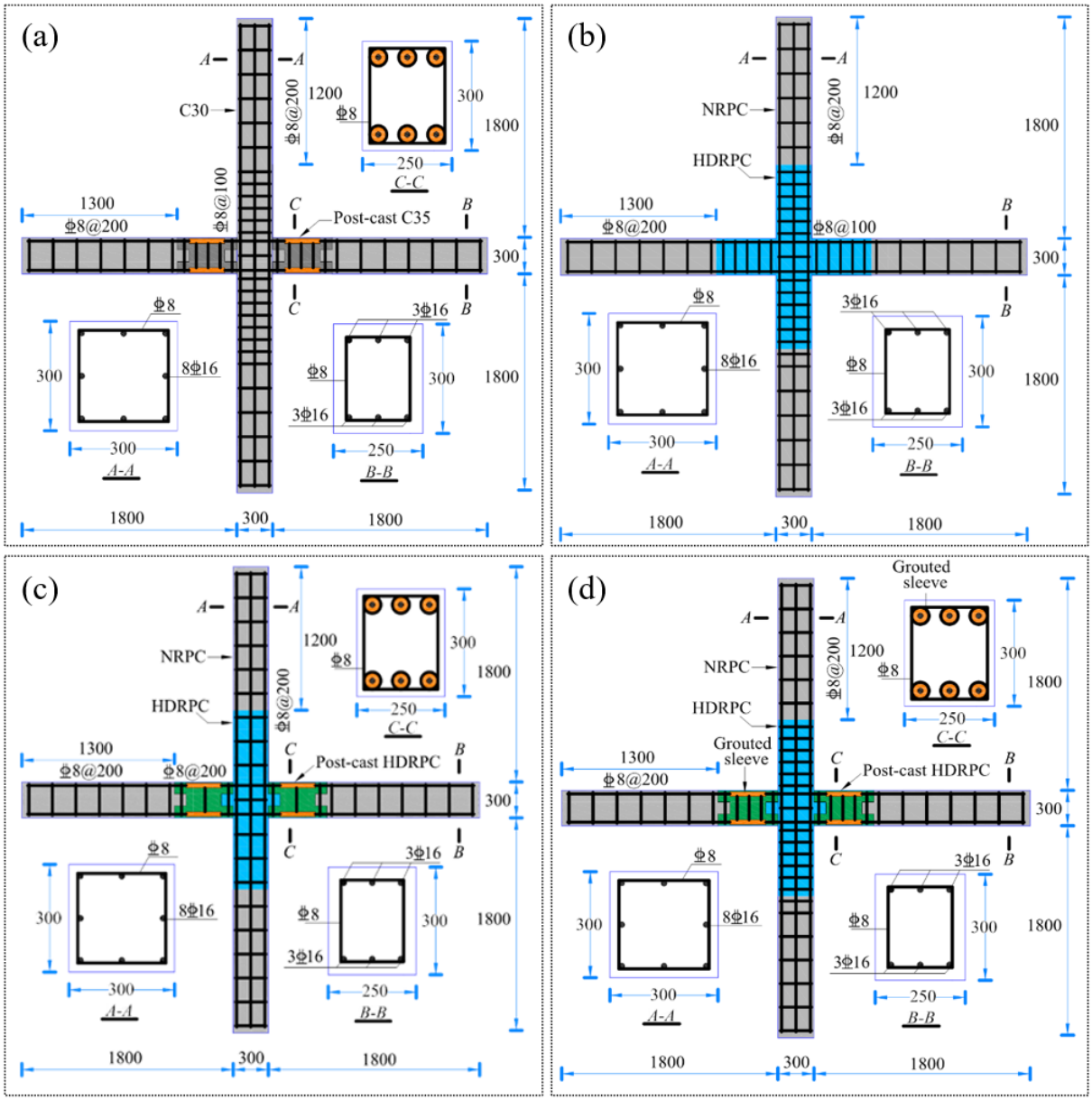


Figure 4. Dimension and details of reinforcements for specimens: (**a**) PC30; (**b**) HDJ; (**c**) PHDJ1; (**d**) PHDJ2-4.

Table 6. Summary of specimens.

Specimens	Construction Method	Materials	Axial Pressure Ratio	Shaft Pressure (kN)	Hoop Arrangement
PC30	precast beam and column assembly	C30	0.3	386.1	⌖ 8@100/200
HDJ	cast-in-place	HDRPC/C30	0.3	386.1	⌖ 8@100/200
PHDJ1	precast beam and column assembly	HDRPC/NRPC	0.3	386.1	⌖ 8@200
PHDJ2		HDRPC/NRPC	0.3	386.1	⌖ 8@100/200
PHDJ3		HDRPC/NRPC	0.5	643.5	⌖ 8@100/200
PHDJ4		HDRPC/NRPC	0.7	900.9	⌖ 8@100/200

For the manufacturing procedure of the assembled joint as shown in Figure 5, firstly the precast parts undergo fabrication and the longitudinal reinforcement spacing is controlled using a limiting template to ensure precise docking of the outstretched reinforcement bars. Additionally, a bubble film is applied to the inner side of the limiting template, which enhances interface roughness and improves the bond strength and flexural performance of the old and new cementitious materials [62]. Then, the sleeve connection is executed. The outstretched reinforcement bars of the prefabricated beams and columns are connected and grouted through the grouting process. Finally, the secondary pouring was conducted to securely attach the formwork for the "I"-shaped back-cast area, remove the bubble film at the keyway interface, and pour the HDRPC.

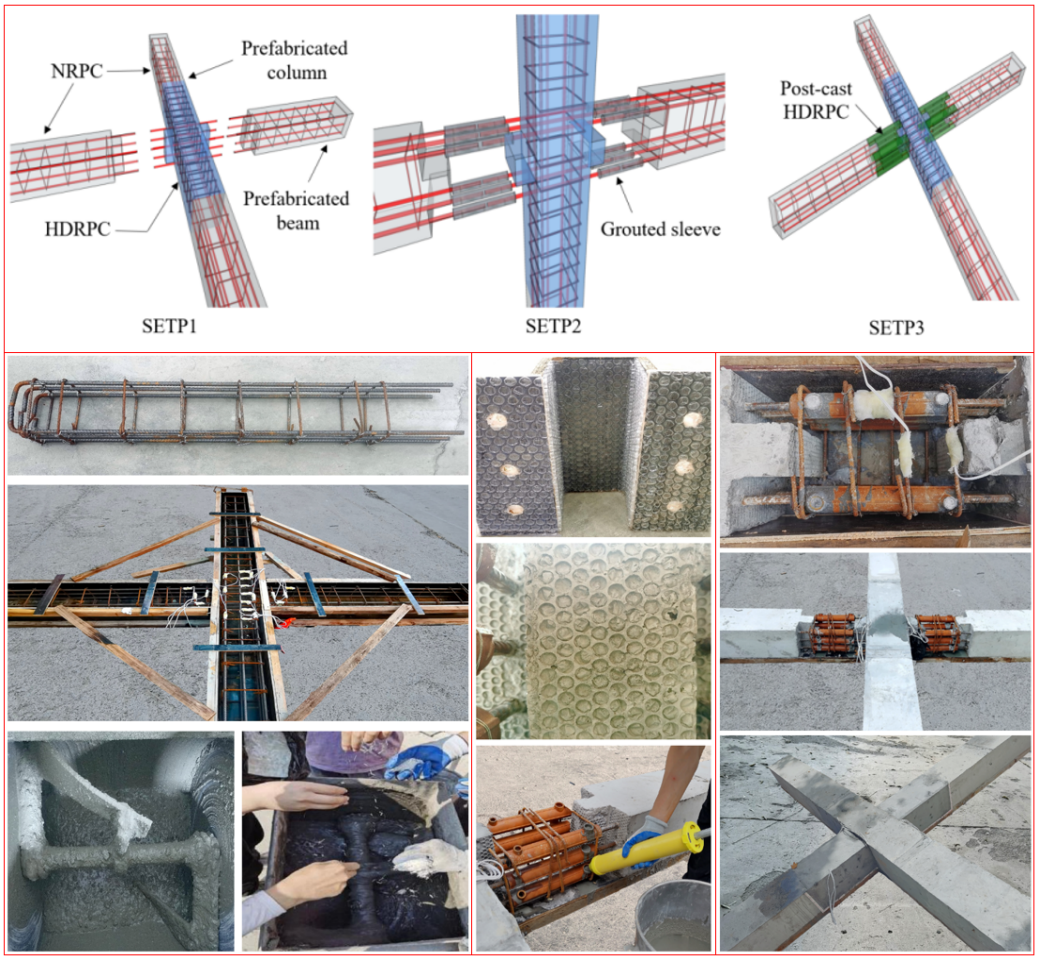


Figure 5. Construction sequence of HDRPC prefabricated beam–column joints.

3.2. Test Setup, Instrumentation, and Loading Protocol

Figure 6 illustrates the experimental setup. The setup consisted of a rigid steel frame anchored to the laboratory floor, which provided the reactive force during loading. The bottom of the column was supported by a 25 mm thick steel plate fixed to a hinge, while the top was constrained by two steel frames to limit lateral displacement. To ensure uniform load distribution and prevent localized deformation, the system incorporated a well-designed load-distribution mechanism. Additionally, hinge points were designed with low friction and zero play to minimize unnecessary deformation. Two MTS actuators, each with a capacity of 250 kN, were connected to the beam ends to apply cyclic loads, while a third actuator, with a capacity of 1000 kN, applied a constant vertical axial load of 386 kN to the top of the column. The system provided high-precision testing capabilities, facilitating a comprehensive evaluation of the mechanical properties of material in a controlled environment. The data-acquisition system ensured real-time synchronization of load, deformation, and force measurements, guaranteeing the accuracy and reliability of the experimental data. Vertical displacement at the beam ends was measured using Linear Variable Differential Transformers (LVDTs), and strain gauges were installed on the longitudinal reinforcement and concrete surface to monitor strain development. The constant axial load, equivalent to 30% of the axial load capacity of the column, was chosen to simulate severe loading conditions typically encountered during seismic events, thereby providing a basis for comparing joint behavior under varying stress levels. This axial load also simulated the effect of gravity load on the column support layer.

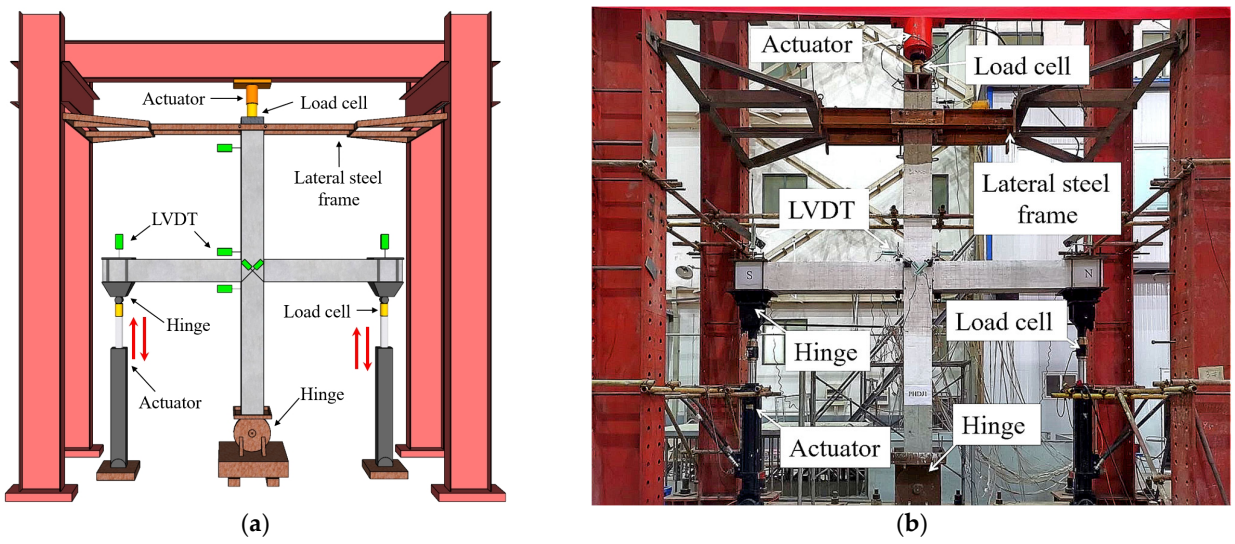


Figure 6. Test setup: (**a**) schematic diagram of loading device; (**b**) loading on-site layout plan.

As shown in Figure 7, strain gauges are placed on both the longitudinal and transverse reinforcement at key locations near the grouting sleeves to measure strain during loading. This configuration enables precise monitoring of the reinforcement response, providing valuable data on joint performance under stress. As depicted in Figure 8, an amplitude-increasing loading scheme is applied to each sample under displacement control. In this scheme, vertical load at the beam end is gradually applied: 4 mm step increments are used before joint yielding, cycled once, while 8 mm step increments are applied after joint yielding, cycled three times. The actuators for the two beams are synchronized: when one actuator pushes a beam upward, the other pulls the opposite beam downward. The test is terminated when the load on either or both actuators drops to 85% of the peak load [60].

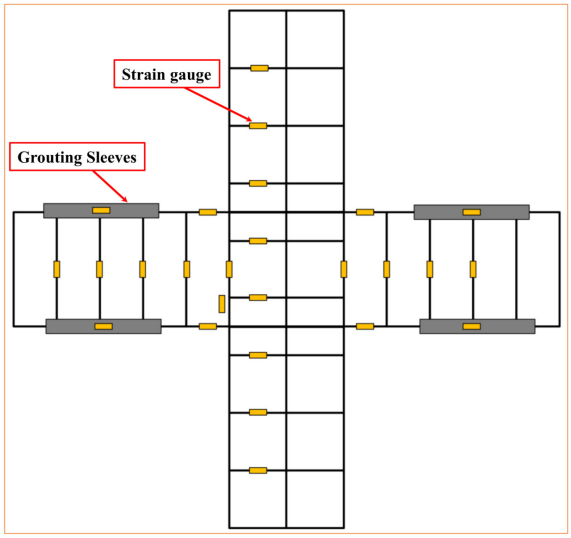


Figure 7. Arrangement of strain gauges.

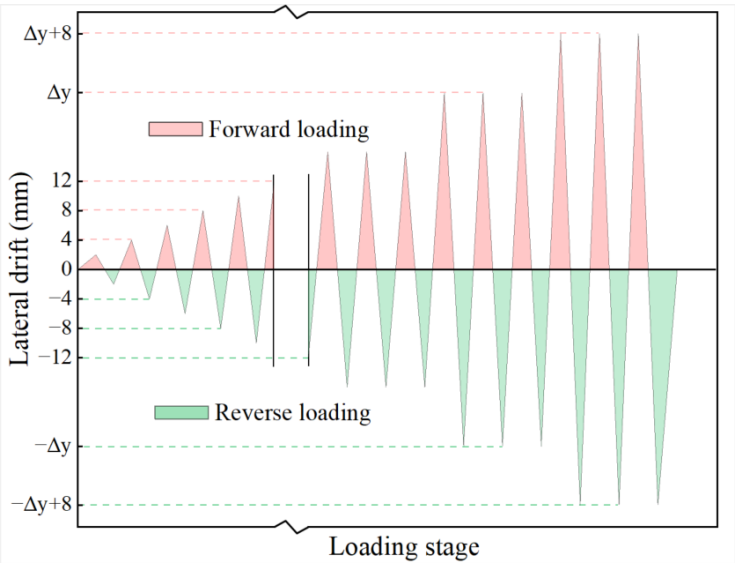


Figure 8. Loading protocol.

4. Main Test Results and Analysis

4.1. Test Phenomena and Failure Characteristics

Figure 9a shows the crack pattern of specimen PC30 made of normal concrete. The failure mode of PC30 is characterized by severe damage, with a displacement of 4 mm near the material contact, causing cracks at the column edge (600 mm from the beam root) and a rapidly propagating 50 mm diagonal core crack. As the displacement increases to 36 mm, transverse cracks appear at the column end, and diagonal cracks (0.2 mm wide) form at the core. Ultimately, the failure is attributed to shear failure, with concrete peeling off at the joints. This type of failure, while observed in the experiment, is typically undesirable in practical structural design. The intention behind designing specimen PC30 in this manner was to investigate the shear failure mechanism in prefabricated concrete joints, which could provide insights into improving joint design for real-world applications.

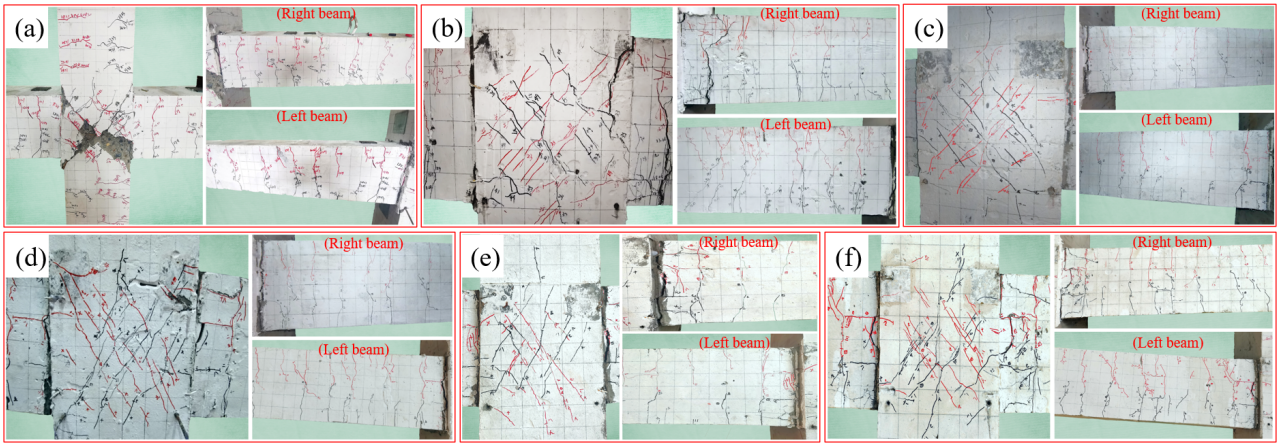


Figure 9. Component failure diagram under cyclic loading: (**a**) crack pattern of PC30 under cyclic loading; (**b**) crack pattern of HDJ under cyclic loading; (**c**) crack pattern of PHDJ1 under cyclic loading; (**d**) crack pattern of PHDJ2 under cyclic loading; (**e**) crack pattern of PHDJ3 under cyclic loading; (**f**) crack pattern of PHDJ4 under cyclic loading.

Figure 9b presents the crack pattern of specimen HDJ made of HDRPC. The crack pattern and hysteresis curve indicate that cracking occurs at all precast joints (PHDJ2-4) in the secondary pouring area, where the precast beams meet. Despite these cracks, the rough surface of the bubble film enhances interfacial adhesion and bending resistance, preventing significant damage. The maximum crack width observed is 0.5 mm, and vertical bending cracks are concentrated approximately 1000 mm from the root to the edge of the beam and column. This suggests that the steel bar joint grouting sleeve method is effective in ensuring sufficient bearing capacity at the connection between prefabricated beams and columns, thereby enhancing mechanical interlocking and delaying premature failure. The initial fracture in HDJ occurs away from the base or joint surface, making it more durable than PHDJ2.

As shown in Figure 9c, increasing the stirrup spacing in HDRPC at the core area from 100 mm to 200 mm results in cracking along the keyway of the I-beam in specimen PHDJ1, which lacks ring reinforcement. The cracks appear in the core region, extending from the upper and lower columns to the central area, with transverse cracks in the keyway reaching 0.5 mm. As displacement increases, concrete bulging and peeling occur. The crack at the bottom of the beam widens significantly to 20 mm under a 128 mm load. The failure mode of PHDJ1 changes from bending to shear failure, attributed to the absence of hoop reinforcement, which leads to plastic deformation at the column end under reciprocating loads. In contrast, specimen PHDJ2, which includes additional longitudinal steel bars, exhibits improved bending strength, thus preventing bending failure before shear failure.

Figure 9d shows that specimen PHDJ2, an HDRPC assembled joint with the same steel reinforcement and structure as PC30, initially cracks at the material interface between the left and right beams, 500 mm from the column edge, when the displacement amplitude reaches 4 mm. As the load increases, diagonal microcracks form in the core, and vertical cracks develop in the post-casting area. When the displacement amplitude reaches 32 mm, the load-displacement curve steepens, indicating joint yielding. At this stage, the crack width peaks at 0.13 mm in the core and 1 mm at the root of the beam. Vertical cracks are evident in the prefabricated beam area, and the base fracture becomes the main crack, widening as the beam end moves. The core crack grows to 0.5 mm, and surface cracks appear on the beam. At a displacement amplitude of 128 mm, the width of the main crack at the root of the beam reaches 17 mm, leading to the collapse of the material in the compression zone and subsequent joint failure. In comparison, specimen PC30 experienced

core shear failure accompanied by concrete detachment, while PHDJ2, although exhibiting minor cracks (with a width of 450 μm), showed no concrete peeling due to the properties of HDRPC.

Finally, comparing Figure 9d–f, the failure modes of three prefabricated joints (PHDJ2-4) with identical steel reinforcement and materials are discussed. As axial compressive force increases, vertical compressive stress in the core area and the angle of diagonal cracks increase. The ultimate load induces the first fracture near the beam foundation at the connection. Subsequent load variations cause the main beam to rotate around both ends, with the grouting sleeve reinforcing the load-bearing capacity at the beam ends.

4.2. Hysteresis Curves

Figure 10 shows the relationship between the applied load on six specimens and the vertical displacement measured from LVDT deployed at the end of the beam. When two actuators load the beam upward and downward relative to the ground, the positive load and negative load (and displacements) correspond to the upward and downward directions. For each specimen, overall, the load-displacement curves of the two beams show the hysteresis curve and the magnitude of the load and deformation.

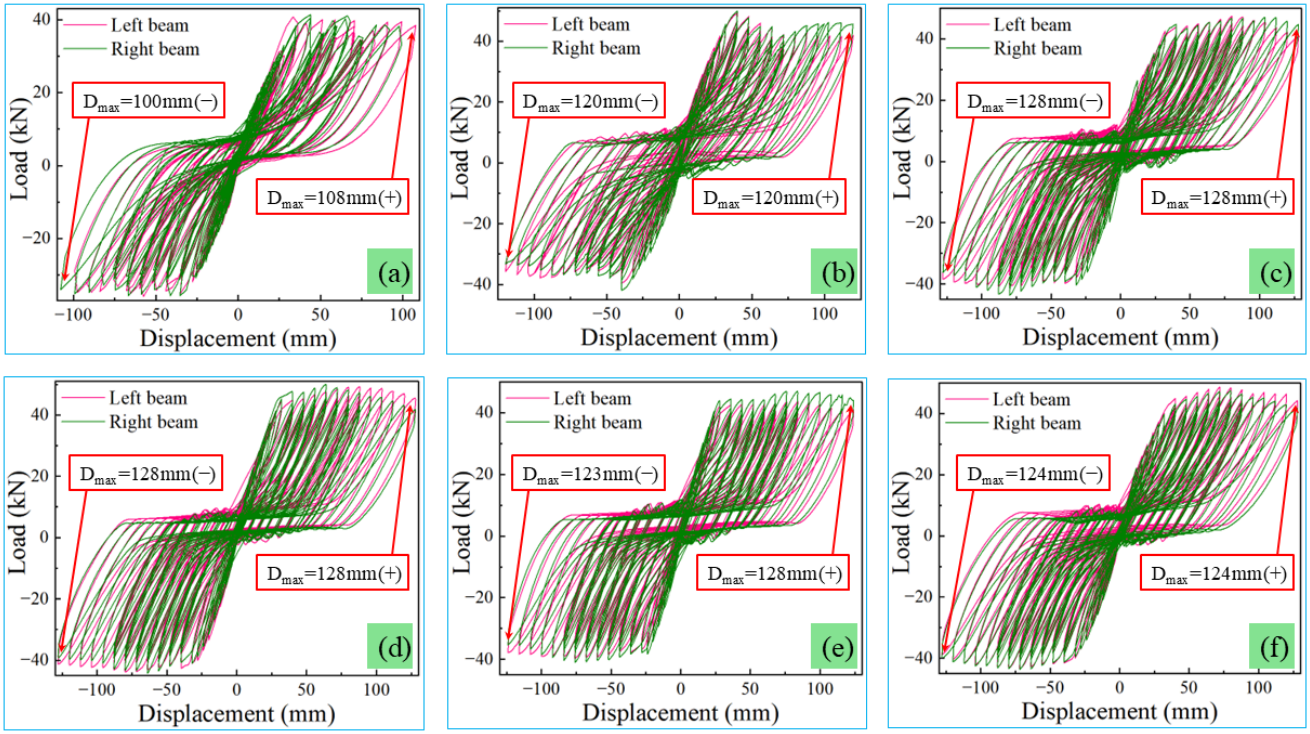


Figure 10. Hysteretic curves of different components: (**a**) P30; (**b**) HDJ; (**c**) PHDJ1; (**d**) PHDJ2; (**e**) PHDJ3; and (**f**) PHDJ4.

Figure 10a shows the load-displacement results of the beams of specimen PC30, respectively. The results indicate that when the displacement amplitude is less than 25 mm, the load during the loading and unloading stages increases approximately linearly with the displacement. When the displacement exceeds 25 mm, the specimen exhibits hysteresis during the loading–unloading phase, which may be due to internal damage such as concrete cracking and steel yield. After the concrete cracks, the magnitude of the load will still increase due to the action of the steel bars. However, the concrete has poor damage resistance and cracks develop rapidly in the core area. Overall, the hysteresis loop of the PC30 joint shows the most obvious shrinkage. In the later stage of loading, plastic hinges are formed at the ends of each joint beam, and the main crack at the root of the beam

alternately opens, closes, and continues to widen under reciprocating loads. The steel bar slip phenomenon is severe, and the hysteresis curve is Z-shaped.

Figure 10b shows the load-displacement results of the beams of specimen HDJ, respectively. Compared with specimen PC30, specimen HDJ has higher bearing capacity, deformation capacity, and hysteresis performance. Before concrete cracking, the load increases approximately linearly with displacement, similar to the results of PC30. After a slight crack appeared at the root of the beam near the column, hysteresis behavior was observed due to damage in the specimen. As the displacement increases, cracks appear at beams and joints far away from the column. However, the size of the load still increases. After the load reaches its peak, it begins to decrease, and when the displacement amplitude reaches 75 mm, the load increases twice. This phenomenon is attributed to the unique tensile and crack resistance of HDRPC. After the cracking of HDRPC, due to the dispersion of mixed fibers in HDRPC, the tensile strain of HDRPC is higher, and it has better-coordinated deformation ability with steel bars. Its excellent crack resistance often hinders the development of damage in HDRPC, thereby reducing the squeezing effect.

Figure 10d shows the load-displacement results of the beams of specimen PHDJ2, respectively. Similar to the HDJ specimen, it exhibits hysteresis behavior and post-cracking resistance. However, overall, the cast-in-place HDJ joint has less shrinkage due to its superior overall integrity compared to prefabricated joints, and the development of crack width at the root of the beam is slower. When fine cracks appear at the root of the side beam of the column, PHDJ2 can still maintain the bearing capacity of the joint and has limited hoop effect, indicating that the design configuration of the prefabricated column and beam enables the assembly joint to achieve reasonable cyclic performance and achieve the same purpose as cast-in-place.

Figure 10c–f show the load-displacement results of the beams of specimens PHDJ1-4, respectively. Under the condition of reducing the reinforcement ratio of stirrups in the core area of the joint, the results of specimen PHDJ2 a high degree of overlap with specimen PHDJ1, indicating that the spacing between stirrups has little effect on the bearing capacity and deformation capacity of the joint. HDRPC itself has good shear performance and can replace some stirrups, which is conducive to simplifying the arrangement of steel bars in the joint area.

4.3. Skeleton Curves and Drift Ratio

The skeleton curve shows the stiffness of component and ductility by correlating force and deformation under alternating load. Individual joint skeletal curves are shown in Figure 10, which shows the joints went through elasticity, yielding, stability, and disintegration. The beam end load and displacement are linear in the elastic stage, and each specimen has a similar initial stiffness. As displacement increases, joint cracks fully develop and internal material damage accumulates, reducing specimen stiffness until yield. HDRPC assembled joint beam end material has a higher ultimate compressive strain in the middle and late stages of loading and benefits from grouting sleeve reinforcement. This keeps bearing capacity stable and improves, lengthening the horizontal segment of the skeleton curve. The bearing capacity of the specimen decreases as the joint beam end material collapses.

The drift ratio is a critical parameter for evaluating the seismic performance of structures, representing the lateral displacement relative to the height of an element. It reflects the deformation capacity of a structure under cyclic loading, indicating its ability to absorb energy and resist damage. Analyzing the drift ratio provides insights into the load-carrying capacity, stability, and overall seismic resilience of various materials and connection types, such as normal concrete and HDRPC, under seismic conditions.

The drift ratio is calculated using the following formula:

$$\text{Drift ratio} = \frac{\Delta}{h} \times 100\% \quad (1)$$

where Δ is the lateral displacement of the top of the beam, measured during cyclic loading, h is the height of the beam. The drift ratio is typically expressed as a percentage, and it helps in assessing the deformation behavior and seismic performance of structural elements, particularly their ability to resist lateral forces without collapsing or undergoing excessive damage.

Figure 11a shows that the elastic phase, HDRPC has a lower elastic modulus than normal concrete, so PC30 joints are stiffer than PHDJ2. The specimen PC30 joints have much lower bearing capacity and stiffness than PHDJ2 during later loading. This is because reciprocating loading weakens concrete, causing cracks and rapid mechanical degradation, while HDRPC has greater crack and energy-dissipation properties than normal concrete.

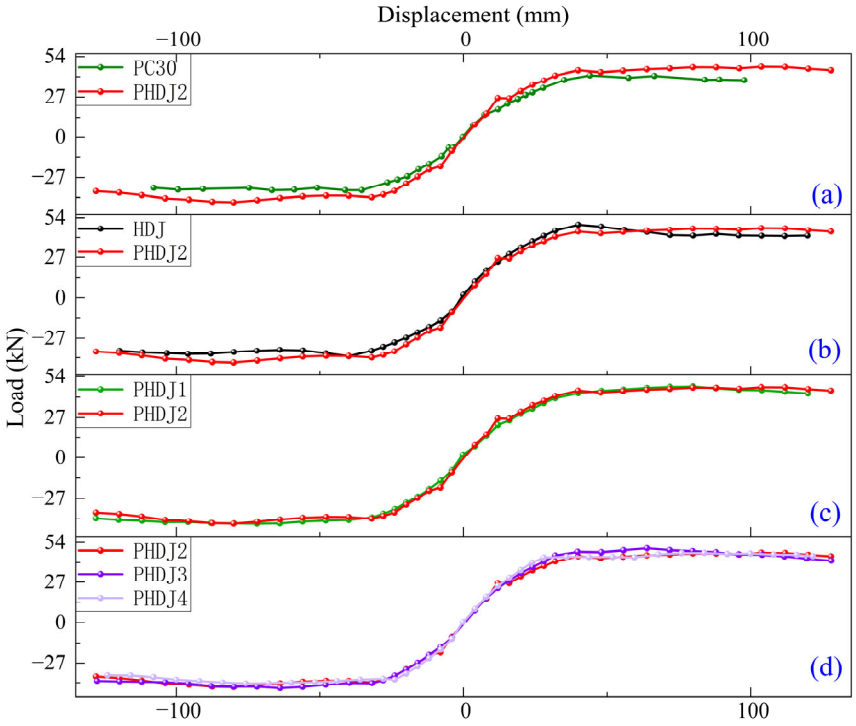


Figure 11. Comparison of skeleton curves and drift ratio: (**a**) different materials; (**b**) different fabrications; (**c**) different hoop ratios; (**d**) different axial compression ratios.

Figure 11b illustrates that the initial stiffness of the HDRPC assembled joint and cast-in-place joint are similar. However, after reaching the peak load, the bearing capacity of the HDJ specimen gradually decreases as the displacement increases. The grouting sleeve at the girder end of the PHDJ2 specimen greatly improves the sectional bending-bearing capacity, resulting in a slight improvement in its bearing capacity initially, followed by a gradual decrease with increasing girder-end displacement. The grouted sleeves with higher stiffness and strength inhibit the propagating and widening of the cracks [35]. Therefore, the PHDJ2 specimen exhibits better ductility compared to the cast-in-place joint.

As shown in Figure 11c, the skeleton curves of specimens PHDJ1 and PHDJ2 exhibit significant overlap. This indicates that the distance between the hoops has a limited influence on the load-bearing and deformation capacity of the joint. Additionally, compared to PC30, PHDJ1 can still maintain a high bearing capacity and load-carrying level while reducing the number of stirrups, HDRPC can replace some of the hoops, simplifying the

reinforcing arrangement in the joint area. This approach addresses the issue of dense and complex reinforcing tying during construction.

Figure 11d indicates that the peak bearing capacity of the joint initially rises and subsequently drops as the axial compression ratio increases. This is because an appropriate axial compression force can widen the compression zone area of the column section, enhance the effectiveness of the inclined compression bar, and improve the shear strength of HDRPC with the increase in compressive stress. However, when the axial compression force becomes severe, the material in the compression zone of the joint will crack, resulting in a drop in shear strength.

The drift ratio analysis of the experimental specimens highlights the significant improvements in seismic performance achieved by HDRPC compared to normal concrete (PC30). The PC30 specimen exhibits a relatively lower deformation capacity, as it demonstrates substantial displacement at smaller drift ratios. In contrast, the HDJ specimen, made of cast-in-place HDRPC, shows a higher load-carrying capacity and offers greater resistance to deformation under cyclic loading. The prefabricated HDRPC specimens (PHDJ1, PHDJ2, PHDJ3, PHDJ4) further outperform both PC30 and HDJ, particularly PHDJ3 and PHDJ4, which exhibit the highest load capacity and maintain consistent performance at higher drift ratios.

International design codes, such as ACI 318 [63] and CEB-FIB [64], typically assume uniform material properties and do not fully account for the enhanced performance of high-ductility materials like HDRPC. For instance, ACI 318 limits the drift ratio to 2% for seismic design, which may be overly conservative for HDRPC joints exhibiting higher ductility. Similarly, the CEB-FIB Model Code lacks specific guidelines for fiber-reinforced concrete joints. These limitations underscore the need for updated design codes that incorporate the unique properties of advanced materials like HDRPC.

4.4. Load Capacity and Ductility

In seismic design, ductility refers to the capacity of structures and members to withstand deformation without a significant decrease in bearing capacity after entering the plastic phase. The ductility coefficient is commonly used to measure the quality of ductility and is calculated using the following formula:

$$\mu = \frac{\Delta_\mu}{\Delta_y} \tag{2}$$

where Δ_u is the ultimate displacement of the beam end of the joint. This refers to the vertical displacement that corresponds to the reduction of the load capacity of the member to 85% of its maximum load capacity. Δ_y, on the other hand, represents the vertical displacement of the beam end of the joint when it reaches its yield point. The yield load was calculated using the farthest point method, where the yield point is defined as the intersection of the initial elastic slope and a line parallel to the post-yield slope passing through the ultimate load point [65]. The displacement ductility coefficients for each joint are listed in Table 5.

As shown in Table 7, the experimental results demonstrate that specimens incorporating HDRPC significantly outperform the PC30 specimen, made of normal concrete, particularly in terms of ultimate load capacity. The influence of concrete strength on ultimate load was investigated by comparing the performance of HDRPC with that of normal concrete. The results reveal that HDRPC increases the ultimate load by 17.8%, underscoring the crucial role of concrete strength in joint performance. Specifically, the HDJ specimen, which uses cast-in-place HDRPC, exhibits a peak load of 49.4 kN in the forward direction and an ultimate load of 41.9 kN, significantly surpassing the PC30 specimen, which has an ultimate load of 38.4 kN in the same direction. The prefabricated HDRPC

specimens (PHDJ1, PHDJ2, PHDJ3, PHDJ4) consistently outperform both the PC30 and HDJ specimens. Notably, PHDJ3 achieves the highest peak load of 50.1 kN in the forward direction and an ultimate load of 42.6 kN, indicating superior seismic performance. The PHDJ4 specimen also demonstrates the highest mean value, showing excellent consistency under reverse loading. These findings confirm that HDRPC, whether cast-in-place or prefabricated, enhances the seismic performance and load-carrying capacity of concrete joints, with concrete strength playing a significant role in improving joint performance.

Table 7. Displacement ductility coefficient.

Specimens	Load Direction	Yield Displacement (mm)	Yield Load (kN)	Peak Load (kN)	Ultimate Load (kN)	Ultimate Displacement (mm)	Mean
PC30	forward	36.0	39.2	40.0	38.4	108	3.0
	backward	28.7	32.3	35.9	34.8	100	3.5
HDJ	forward	30.3	43.9	49.4	41.9	120	4.0
	backward	30.8	35.0	39.5	35.7	120	3.9
PHDJ1	forward	31.9	39.8	47.5	41.7	128	4.0
	backward	31.9	39.5	43.7	40.0	128	4.0
PHDJ2	forward	32.0	41.3	47.1	44.7	128	4.0
	backward	28.0	38.5	43.6	37.0	128	4.3
PHDJ3	forward	31.9	45.3	50.1	42.6	123	3.9
	backward	28.1	38.9	44.3	39.3	128	4.5
PHDJ4	forward	28.0	43.9	47.0	44.8	124	4.3
	backward	24.0	38.3	41.0	35.3	124	5.1

Based on the provided table, it is evident that the displacement ductility coefficients of HDRPC joints are considerably greater than those of assembled concrete joints. This suggests that incorporating HDRPC materials in the core is beneficial for enhancing the joint damage pattern, increasing the joint load-carrying capacity, and improving the joint ductility. The ductility of HDRPC assembled joints is typically greater than that of the HDJ cast-in-place joints, indicating that the grouted sleeve connection in its assembled form can enhance the ductility of the girder cross-section. When comparing PHDJ2 with PHDJ1, it was found that the ductility of PHDJ1 joints with unencrypted hoop reinforcement was slightly decreased. However, it still reached a value of 4.0, which suggests that the excellent shear ductility of the material can serve a similar purpose as the hoop reinforcement in terms of shear and restraint.

4.5. Stiffness Degradation

The stiffness and bearing capacity of the joint gradually decrease under the reciprocating load. To measure the change in stiffness of the specimen at different loading displacements, the cut-line stiffness K_i [64] is commonly utilized. The stiffness degradation curve of the joint is determined for the right beam, as shown in Figure 11.

$$K_i = \frac{|+F_i| + |-F_i|}{|+X_i| + |-X_i|} \tag{3}$$

where K_i represents the secant stiffness of the i^{th} loading level; $+F_i$ and $-F_i$ represent the positive and negative peak loads corresponding to the i^{th} loading level; $+X_i$ and $-X_i$ represent the displacement toward the positive and negative peak loads corresponding to the i^{th} loading level.

As shown in Figure 12, before reaching the yield state, the overall stiffness trend of the six specimens rapidly decreases with increasing displacement. After yielding, the rate of stiffness degradation slows down, and the curve tends to flatten as it approaches the limit state.

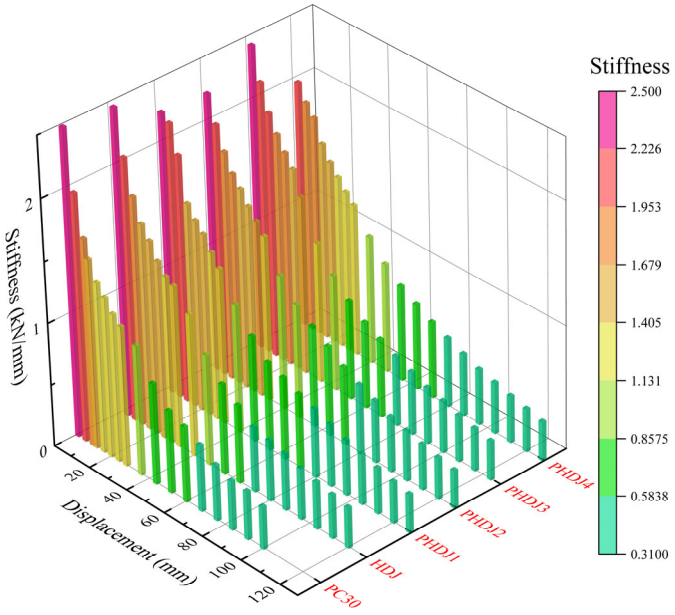


Figure 12. Results of stiffness degradation.

Compared with PHDJ2 precast joints, normal concrete precast joints PC30 have higher initial stiffness but a faster degradation rate. The main reason is that HDRPC does not contain coarse aggregates and has a lower elastic modulus than normal concrete. However, as displacement increases, concrete cracks under tensile action, rapidly develop and accumulate plastic damage. The stiffness of normal concrete joints rapidly decreases, while the tensile strength and ultimate tensile strain of HDRPC are much higher than those of concrete. Therefore, the rate of stiffness reduction is slower, resulting in a higher final stiffness.

The HDJ specimen is a cast-in-place integral joint; however, there is a weak interface caused by secondary pouring in the assembly joint specimen PHDJ2. At the initial stage of loading, there will be varying degrees of cracking at the connection between the post-cast area of specimen PHDJ2 and the prefabricated beam. Therefore, HDJ joints have higher initial stiffness. As the displacement increases, cracks in both specimen HDJ and specimen PHDJ2 fully develop, and the stiffness degradation curves of the two joints become similar. In the later stage of loading, both specimen beam ends showed significant plasticity. However, due to the larger cross-sectional area of the grouting sleeve, it can serve as a form of local reinforcement, and the ultimate stiffness of specimen PHDJ2 is slightly higher than that of the HDJ specimen.

When comparing specimens with different axial compression ratios (PHDJ2-4), it was observed that the stiffness degradation curves of PHDJ2 and PHDJ3 with lower axial compression ratios were similar to each other. However, PHDJ4 with a high axial compression ratio exhibits significantly higher initial stiffness. At the limit state, the final stiffness of all three joints is similar, indicating that the degradation rate of the joints is faster under high axial compression ratios. PHDJ1 has the lowest initial stiffness, indicating that the constraint force at the beam end is weakened and the interface is more prone to cracking when the spacing between the circumferential steel bars is wide.

4.6. Energy-Consumption Capacity

The structure will fracture and deform under seismic forces, thereby dissipating and absorbing seismic energy. Hysteretic energy dissipation is advantageous for mitigating the displacement response of a structure during seismic activity and enhancing its seismic performance. The energy-consumption capacity of each specimen was calculated by

integrating the area under the load-displacement hysteresis loops. This represents the cumulative energy dissipated during cyclic loading, which is a key indicator of seismic performance. The hysteresis energy-dissipation curve is constructed by plotting the energy dissipation of the first cycle at each loading stage, as depicted in Figure 13.

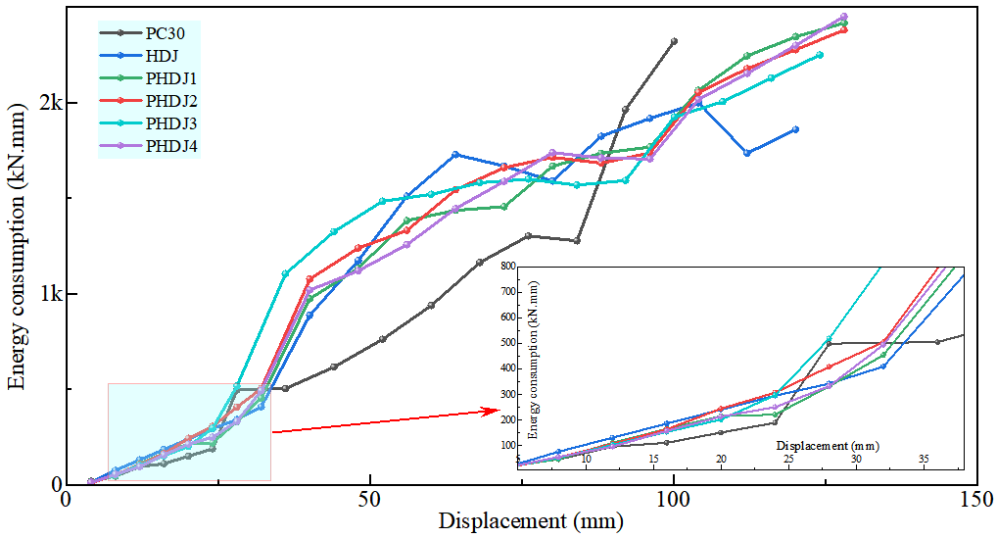


Figure 13. Energy-dissipation capacity of specimens.

During the initial loading phase, each specimen remains primarily in the elastic stage, with minimal and gradual energy dissipation, which remains relatively consistent across all specimens. However, once the yield displacement is reached, hysteresis energy dissipation at the joints increases rapidly as the load increases. Concrete exhibits limited resistance to damage, and as internal cracks develop, both its strength and stiffness decrease significantly. Consequently, the energy-dissipation capacity of PC30 joints is much lower than that of HDRPC joints after reaching the yield point. As shown in Figure 13, the energy consumption of the PC30 specimen increases sharply beyond 80 mm of displacement. This substantial rise in energy dissipation is attributed to the brittle failure behavior of normal concrete. Once cracks form, the stiffness of material rapidly decreases, leading to accelerated energy consumption. In contrast, HDRPC demonstrates superior crack resistance and ductility, resulting in more stable energy dissipation at larger displacements. During the later stages of loading, the beam end undergoes plastic deformation and forms a plastic hinge, which becomes the primary region for energy dissipation. The energy-dissipation effect of the grouting sleeve at the beam end of the assembly joint is evident, resulting in a higher level of energy dissipation compared to the cast-in-place joint. The energy-consumption patterns of PHDJ1 and PHDJ4 are similar, suggesting that increasing the hoop spacing does not reduce the energy-dissipation level of the HDRPC assembly joint.

4.7. Core Area Shear Deformation

Under reciprocating load, the core area of the joint experiences shear deformation, resulting in tensile stress along one diagonal direction and compressive stress along the other diagonal direction. Figure 13 illustrates how the core area tends to shift from a rectangle to a rhombus, with the direction of the rhombus alternating with each application of the beam end load. The extent of shear deformation in the core area can be evaluated by the shear angle. Equations (4) and (5) provide formulas for calculating the shear angle.

$$\overline{X} = \frac{|\delta_1 + \delta_1'| + |\delta_2 + \delta_2'|}{2} \tag{4}$$

$$\gamma = \frac{\sqrt{a^2 + b^2}}{a \cdot b} \cdot \overline{X} \tag{5}$$

where $\overline{X}$ is the average change in the diagonal direction of the core area, and γ represents the shear angle of the core area. The remaining variables are detailed in Figure 14, and the calculation results are presented in Figure 15.

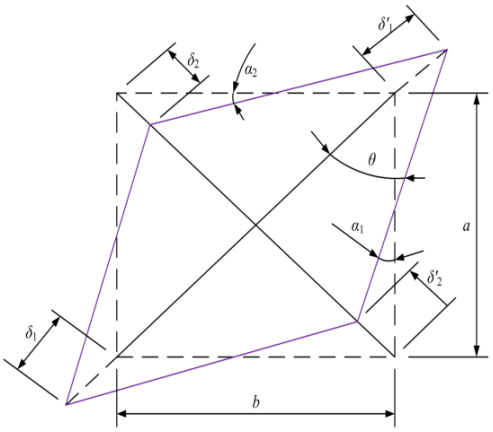


Figure 14. Shear deformation in the joint core.

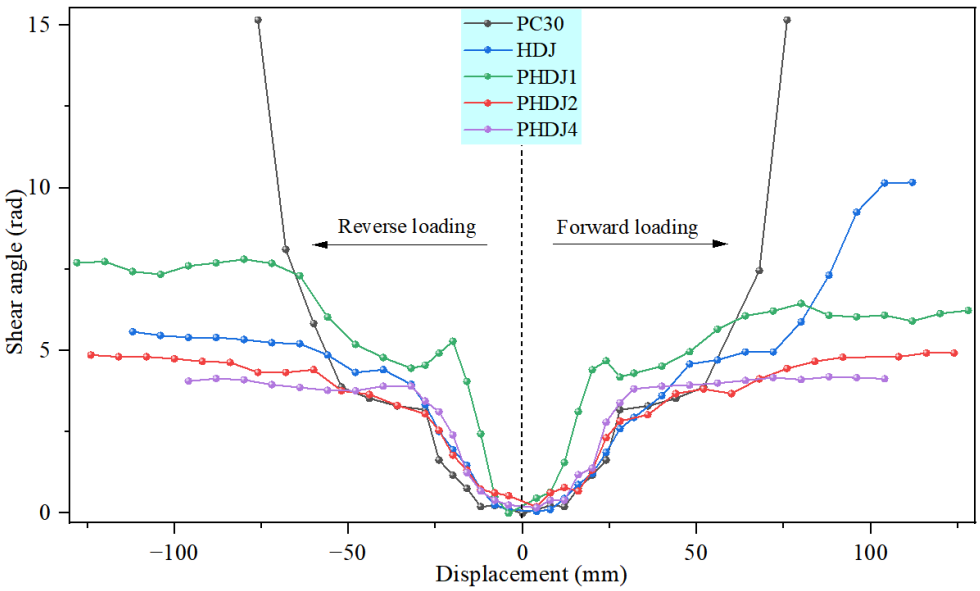


Figure 15. Shear angle of the joint core.

Figure 15 illustrates that during the initial loading phase, the shear deformation in the core region of each specimen is minimal, and the curves closely align with each other. However, as the displacement at the beam end increases, noticeable concrete cracking occurs in the core area of the PC30 joint. The growth rate and peak value of the shear angle in this joint are significantly higher compared to the other joints. The shear angle of PHDJ1, PHDJ2, and HDJ increases gradually after complete cracking in the core, reaching a maximum value that is only one-third of that observed in the PC30 joint. Because the addition of PVA fibers and basalt fibers in HDRPC helps establish bridging connections and promote stress transfer, replacing HDRPC at the joint exhibits enhanced shear ductility and maintains steady-state cracking characteristics [31]. The experimental strain readings were compared with analytical values calculated using the sectional equilibrium method. The results showed good agreement, with a maximum deviation of 5% in the joint core

area. The shear angle of PHDJ1 in the core is approximately 1.5 times more than that of PHDJ4, suggesting that the spacing between the hoops has a stronger impact on the shear deformation of the joint. However, it is still less than half of the shear angle observed in the PC30 joint, indicating that PHDJ1 performs better than the completed concrete joint.

4.8. Load Capacity of Crack Resistant

Certain reinforced concrete frame structures have special requirements for durability under normal conditions of use and need to avoid cracking. Su et al. [66] have been given the derivation process and general form of the formula for calculating the cracking capacity of joints:

$$V_{j,cr} = f_{tk} b_j h_j \sqrt{1 + \frac{N_c}{f_{tk} b_c h_c}} \tag{6}$$

where $V_{j,cr}$ is the joint shear force when the core area cracks first; b_j is the effective width of the joint core area section; h_j is the height of the joint core area section; N_c is the axial force transmitted by the column; b_c is the column section width; h_c is the column section height. In the case of HDRPC, f_{tk} is the initial cracking stress of the dumbbell-shaped pull plate in the uniaxial tensile test, with an actual test measurement of $f_{tk} = 3.5$ MPa. The tensile strength design value for concrete is approximately considered.

Practically, the bond stress between the longitudinal reinforcement of the beam and the cementitious material in the core area of the joint is unevenly distributed [60]. As a result, the horizontal shear stress transferred to the core area of the joint is also uneven. To account for this, a comprehensive influence coefficient η needs to be introduced for correction, based on theoretical formulas [35]. When considering HDRPC joints, it is important to take into account the positive impact of incorporating PVA fibers and basalt fibers in the material, which improves fracture resistance. Conversely, the negative impact of using recycled powder should also be addressed.

The initial shear force test values of joints are generally lower than the calculated values. According to the calculation results in the table, the comprehensive influence coefficient η = 0.75 can be conservatively taken in the design application, The test value of shear force at the initial cracking of the joint is calculated by the following Equation (7) [67]:

$$V_j = \frac{\sum M_b}{h_0 - a_s'} \left(1 - \frac{h_0 - a_s'}{H_c - h_b}\right) \tag{7}$$

where $\sum M_b$ is the total of the bending moments at the ends of the beam when the joint experiences cracking; h_0 is the effective height of the beam section; a_s' is the distance from the point where the longitudinal reinforcement of the beam intersects to the edge of the section; H_c is the overall height of the column; and h_b is the height of the beam section.

Utilize Equations (6) and (7) to compute the estimated value and test value, respectively, for the fracture-resistance carrying capacity of the core area of each joint. The outcomes are presented in Table 8.

According to the calculation results in Table 6, it can be seen that the tensile strength of specimen PC30 normal concrete is poor, and its initial crack load is significantly lower than other specimens. The initial shear force of specimen PHDJ2-4 increases with the increase in of axial compression ratio. This is because the increase of axial compression increases the compression zone area of the column, delaying the occurrence of diagonal tensile cracks. When the axial compression ratio is the same, the initial cracking loads of PHDJ1, PHDJ2, and HDJ are close, indicating that the prefabricated joints connected by grouting sleeves can achieve the same crack resistance as cast-in-place joints, and the lack of reinforcement has no adverse effect on the initial cracking of the joints. The initial shear force test values of joints are generally lower than the calculated values. According to the calculation results in

Table 6, the comprehensive influence coefficient η = 0.75 can be conservatively taken in the design and application. It is recommended that the formula for the crack-resistance-bearing capacity of the HDRPC joint oblique section be:

$$V_{j,cr} = 0.75 f_{tk} b_j h_j \sqrt{1 + \frac{N_c}{f_{tk} b_c h_c}} \tag{8}$$

Table 8. Load capacity of crack resistance (unit: kN).

Specimens	Load Direction	Incipient Crack Load, P_{cr}	Initial Cracking Shear Test Value $V_{j,exp}$	The Calculated Value of Initial Cracking Shear $V_{j,cal}$	$V_{j,exp}/V_{j,cal}$
PC30	forward	13.9	226.4	257.4	0.88
	backward	16.8	273.6		1.06
HDJ	forward	23.3	379.5	469.9	0.81
	backward	24.3	395.8		0.84
PHDJ1	forward	22.2	364.1	469.9	0.77
	backward	25.8	423.2		0.90
PHDJ2	forward	23.7	388.9	469.9	0.83
	backward	24.5	401.9		0.86
PHDJ3	forward	28.2	462.9	549.3	0.84
	backward	31.5	516.7		0.94
PHDJ4	forward	30.2	495.5	618.9	0.80
	backward	29.3	480.6		0.78

4.9. Shear-Bearing Capacity

Hwang and Lee [68] proposed a Softened Strut-and-Tie (SST) model to calculate the shear strength of external beam–column joints. This model has a clear transmission path and mechanism, dividing the force-bearing mechanism of the joint area into three parts: oblique, vertical, and horizontal as shown in Figure 16. The calculation formula for the shear-bearing capacity of the joint is:

$$V_j = K\zeta f_c' A_{str} \cos\theta \tag{9}$$

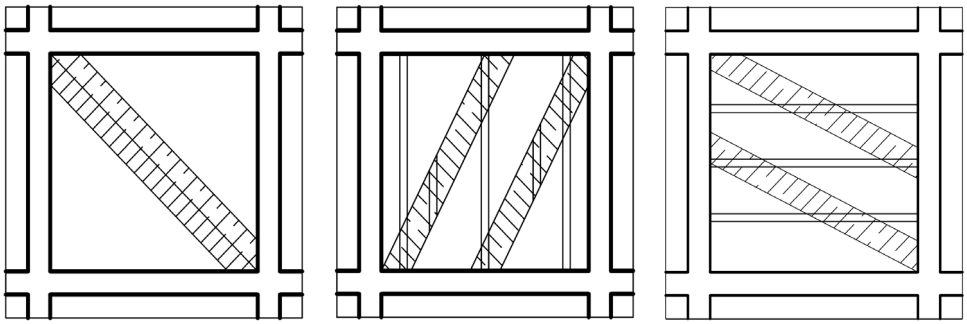
where K is the coefficient of the softened tension rod compression rod model; ζ is the softening coefficient of compressive strength of concrete; f_c' is the compressive strength of cylindrical concrete, taken as $f_c' = 0.79 f_{cu}$; A_{str} is the effective area of the diagonal strut; θ is the angle between the diagonal strut and the horizontal direction.

$$A_{str} = a_s \times b_s \tag{10}$$

where a_s is the effective cross-sectional height of the diagonal strut, b_s is the effective cross-sectional width of the diagonal compression bar, which can be taken as the effective width of the joint b_j.

$$a_s = \sqrt{a_b^2 + a_c^2} \tag{11}$$

where a_b is the height of the compression zone of the beam section, a_c is the height of the compression zone of the column section.



(**a**) (**b**) (**c**)

Figure 16. The theory of SST model: (**a**) diagonal; (**b**) vertical; (**c**) horizontal.

In this experiment, under the action of reciprocating loads, plastic hinges were formed at the ends of the beams on both sides of the core area, and the root of the beam cracked under tension. The neutral axis of the section moved upward, and the relative height of the compression zone decreased. a_b can be approximately taken as one-fifth of the height of the beam section [69]; a_c is determined based on axial pressure, and the calculation formula is:

$$a_c = \left(0.25 + 0.85\frac{N}{b_c h_c f_c'}\right) h_c \tag{12}$$

When appropriate axial pressure is applied to the top of the column, the effective cross-sectional height of the diagonal brace will increase, which is beneficial for the shear resistance of the joint. However, excessive axial pressure will exacerbate the damage to the concrete in the core area, which is unfavorable for shear resistance.

$$\theta = \tan^{-1}\left(\frac{h_b''}{h_c - 2a_c/3}\right) \tag{13}$$

where h_b'' is the distance between the centerline of the outermost longitudinal reinforcement of the beam section.

$$\zeta = 3.35/\sqrt{f_c'} \tag{14}$$

$$K = K_h + K_v - 1 \tag{15}$$

$$K_h = 1 + \frac{\left(\overline{K_h} - 1\right) A_{th} f_{yh}}{\overline{F_h}} \leq \overline{K_h} \tag{16}$$

$$K_v = 1 + \frac{\left(\overline{K_v} - 1\right) A_{tv} f_{yv}}{\overline{F_v}} \leq \overline{K_v} \tag{17}$$

$$\overline{K_h} = \frac{1}{1 - 0.2\left(\gamma_h - \gamma_h^2\right)} \tag{18}$$

$$\overline{K_v} = \frac{1}{1 - 0.2\left(\gamma_v - \gamma_v^2\right)} \tag{19}$$

where A_{th} is the total cross-sectional area of the longitudinal reinforcement in the column; A_{tv} is the total cross-sectional area of the hoop reinforcement along the horizontal loading direction within the core area of the column; f_{yh} is the yield strength of the longitudinal reinforcement of the column; f_{yv} is the yield strength of the hoop reinforcement in the core area of the column; γ_h represents the proportion of horizontal tie rod shear force to the total shear force of the joint; γ_v is the proportion of vertical tension rod shear force to the total

shear force of the joint. $\overline{F_h}$ is the balance tension of the horizontal pull rod; $\overline{F_v}$ is the balance tension of the vertical pull rod.

$$\gamma_h = \frac{2tan\theta - 1}{3} \tag{20}$$

$$\gamma_v = \frac{2cot\theta - 1}{3} \tag{21}$$

$$\overline{F_h} = \gamma_h \overline{K_h} \zeta f_c' a_s b_j cos\theta \tag{22}$$

$$\overline{F_v} = \gamma_v \overline{K_V} \zeta f_c' a_s b_j sin\theta \tag{23}$$

The standard GB 50011-2010 [61] is founded on the truss shear mechanism and accounts for the transfer of shear force to the frame joints through the concrete diagonal compression bars. This includes the axial force of the concrete and columns between the diagonal cracks in the core area. Additionally, the horizontal hoops exert a restraining influence on the diagonal compression bars in the joint region. The calculation of this effect is determined by the following formula:

$$V_j = \frac{1}{\gamma_{RE}} \left(1.1 \eta_j f_t b_j h_j + 0.05 \eta_j N \frac{b_j}{b_c} + f_{yv} A_{svj} \frac{h_{b0} - a_s'}{s} \right) \tag{24}$$

where γ_{RE} is the seismic adjustment coefficient of bearing capacity and is assigned a value of 0.85. η_j is the influence coefficient of orthogonal beam constraints, assigned a value of 1.0. N is the axial pressure of the column. A_{svj} is the total cross-sectional area of the hoop reinforcement within the valid check width of the core area, in the same direction and with the same cross-section.

The test value of nodal shear is determined by measuring the beam end load at the core during cracking and then substituted into Equation (7). The theoretical value of shear capacity is obtained using Equation (24). The resulting values are presented in Table 9. The calculation results indicate that the test value of nodal capacity, obtained by applying the design formulas specified, closely aligns with the calculated value. The ratio between the two has a mean value of 1.03, with a standard deviation and coefficient of variation of 0.05.

Table 9. Comparison of test and calculated values (unit: kN).

Specimen	Load Direction	Left Beam Load	Right Beam Load	Shear Test Value V_{exp}	Normative Formula Calculated Value V_{cal}	V_{exp}/V_{cal}
PC30	forward	30.8	30.4	450.5	469.9	0.96
	backward	30.2	31.8	456.4		0.97
HDJ	forward	39.5	43.3	609.6	586.4	1.04
	backward	38.3	45.5	616.9		1.05
PHDJ1	forward	39.9	39.8	586.7	537.5	1.09
	backward	40.2	39.6	587.5		1.09
PHDJ2	forward	39.8	44.8	622.8	586.4	1.06
	backward	39.2	43.9	611.8		1.04
PHDJ3	forward	42.8	47.7	666.3	601.6	1.11
	backward	44.9	40.9	631.6		1.05
PHDJ4	forward	37.8	44.5	605.9	616.7	0.98
	backward	42.6	38.3	595.6		0.97

5. Conclusions

This study investigated the cyclic behavior of prefabricated beam–column joints using high-ductility recycled powder concrete (HDRPC) under low-cycle reversed loading. The

experimental results and theoretical analyses provide valuable insights into the seismic performance of HDRPC joints, with the following key conclusions:

(1) HDRPC significantly improves the seismic performance of prefabricated joints compared to normal concrete. The bearing capacity of HDRPC joints increased by 17.8%, and the displacement ductility improved by 33.3%. This is attributed to the superior crack resistance and energy-dissipation properties of HDRPC, which mitigate damage in the joint core area and delay failure. The use of HDRPC in the joint core area resulted in multi-crack steady-state cracking, reducing crack widths and shear deformation. This behavior is critical for achieving robust joint designs in earthquake-prone regions.

(2) The grouting sleeve connection method proved highly effective in ensuring reliable force transfer between prefabricated beams and columns. It enhanced the bending capacity of the joint cross-section, allowing for better rotation of the plastic hinge zone at the beam end. The skeleton curves of HDRPC joints exhibited longer horizontal segments and gradual degradation, indicating improved ductility and energy dissipation compared to cast-in-place joints. This demonstrates that grouting sleeves are a superior connection method for prefabricated structures.

(3) Increasing the axial compression ratio improved the cracking load of HDRPC joints but accelerated stiffness degradation. The shear capacity initially increased with higher axial compression but decreased under excessive axial pressure due to concrete damage in the compression zone. Despite these variations, HDRPC joints maintained excellent ductility across the tested range of axial compression ratios (0.3 to 0.7), making them suitable for a wide range of structural applications.

(4) HDRPC joints with reduced hoop reinforcement (e.g., PHDJ1 with 200 mm spacing) exhibited superior performance compared to normal concrete joints with densified stirrups. This suggests that HDRPC can partially replace hoop reinforcement, simplifying steel reinforcement arrangements and addressing construction challenges related to dense reinforcement tying.

(5) The proposed crack-resistance-bearing capacity formula is closely aligned with experimental results, providing a reliable design tool for HDRPC joints. The Softened Strut-and-Tie Model (SST) and normative formula (GB 50011-2010) accurately predicted the shear capacity of HDRPC joints, with a mean ratio of test-to-calculated values of 1.03 and a standard deviation of 0.05.

Author Contributions: Conceptualization, X.L.; Methodology, X.L. and H.S.; Software, X.L. and K.C.; Formal analysis, X.L.; Investigation, X.L., H.S., K.C., T.Y., L.W., X.Z. and T.B.; Resources, X.L.; Data curation, X.L., H.S. and K.C.; Writing—original draft, H.S. and K.C.; Writing—review and editing, X.L., T.Y., L.W., X.Z. and T.B.; Supervision, X.L.; Project administration, X.L.; Funding acquisition, X.L. All authors have read and agreed to the published version of the manuscript.

Funding: This research was funded by the National Natural Science Foundation of China [grant No. 52278507]; the Natural Science Foundation of Shandong Province [grant No. ZR2020ME245]; and the Major Scientific & Technological Innovation Project of Shandong Province [grant No. 2021CXGC011204).

Data Availability Statement: The original contributions presented in the study are included in the article, further inquiries can be directed to the corresponding author.

Conflicts of Interest: The authors declare that we have no known competing financial interests or personal relationships that could have appeared to influence the work reported in this paper.

References

1. Hassan, Y.; Shankar, V.; Usman, S.; Alhassan, A. Carbon footprint management: A review of construction industry. *Clean. Eng. Technol.* **2022**, *9*, 100531.
2. Zhao, Y.; Wang, T.; Yi, W. Emergy-accounting-based comparison of carbon emissions of solid waste recycled concrete. *Constr. Build. Mater.* **2023**, *387*, 131674. [CrossRef]
3. Azarbayjani, M.; Thaddeus, D. *Environmental Dimensions of Climate Change: Endurance and Change in Material Culture*; Springer International Publishing: Berlin/Heidelberg, Germany, 2022; pp. 293–371.
4. Xiao, J.; Ma, Z.; Sui, T.; Akbarnezhad, A.; Duan, Z. Mechanical properties of concrete mixed with recycled powder produced from construction and demolition waste. *J. Clean. Prod.* **2018**, *188*, 720–731. [CrossRef]
5. Wu, K.; Wang, Z.; Jin, W.; Wang, W. Quantitative analysis of the sustainable cost of prefabricated concrete structures. *J. Build. Struct.* **2021**, *42*, 133–144. [CrossRef]
6. Marco, C.; Frappa, G.; Sabbà, M.; Campione Pauletta, M. Shear strength formula for interior beam-column joints with plain bars in existing buildings. *Eng. Struct.* **2023**, *293*, 116656. [CrossRef]
7. Kalogeropoulos, G.; Tsonos, A.-D.; Iakovidis, P. Hysteresis Behavior of RC Beam–Column Joints of Existing Substandard RC Structures Subjected to Seismic Loading–Experimental and Analytical Investigation. *Buildings* **2024**, *14*, 1609. [CrossRef]
8. Zhuang, M.-L.; Sun, C.; Yang, Z.; An, R.; Bai, L.; Han, Y.; Bao, G. Numerical Investigation on the Seismic Behavior of Novel Precast Beam–Column Joints with Mechanical Connections. *Buildings* **2024**, *14*, 1199. [CrossRef]
9. Pekgokgoz, R.K.; Yakut, I. Investigation of Passive Controlled Post-Tensioning System on the Structural Behaviour of Precast Reinforced Concrete Beam–Column Connections. *Buildings* **2024**, *14*, 3910. [CrossRef]
10. Feng, S.; Yang, Y.; Xue, Y.; Yu, Y. Numerical Investigation on the Hysteretic Performance of Self-Centering Precast Steel–Concrete Hybrid Frame. *Buildings* **2024**, *14*, 3202. [CrossRef]
11. Xiao, J.; Ma, X.; Liu, Q.; Zhang, H.; Duan, Z. Evolvement and research progress of concept for full recycled concrete. *J. Archit. Civ. Eng.* **2021**, *38*, 1–15. [CrossRef]
12. Tam, V.; Soomro, M.; Evangelista, A. A review of recycled aggregate in concrete applications (2000–2017). *Constr. Build. Mater.* **2018**, *172*, 272–292. [CrossRef]
13. Li, Q.; Yue, G.; Guo, Y. *Property Regulation and Mix Proportion Design of Recycled Concrete*; China Architecture & Building Press: Beijing, China, 2019; pp. 1–8.
14. Schoon, J.; De Buysser, K.; Van Driessche, I.; De Belie, N. Fines extracted from recycled concrete as alternative raw material for Portland cement clinker production. *Cem. Concr. Compos.* **2015**, *58*, 70–80. [CrossRef]
15. Lin, Y.; He, T.; Da, Y.; Yang, R.; Zheng, D. Effects of recycled powders mixing methods on the properties of recycled concrete. *J. Build. Eng.* **2023**, *80*, 107994. [CrossRef]
16. Zhang, D.; Zhang, S.; Huang, B.; Yang, Q.; Li, J. Comparison of mechanical, chemical, and thermal activation methods on the utilisation of recycled concrete powder from construction and demolition waste. *J. Build. Eng.* **2022**, *61*, 105295. [CrossRef]
17. Li, Z.; Bian, Y.; Zhao, J.; Wang, Y.; Yuan, Z. Recycled concrete fine powder (RFP) as cement partial replacement: Influences on the physical properties, hydration characteristics, and microstructure of blended cement. *J. Build. Eng.* **2022**, *62*, 105326. [CrossRef]
18. Yu, J.; Jiang, F.; Yu, K.; Dong, F.; Duan, X. Deformability enhancement of fiber-reinforced cementitious composite by incorporating recycled powder. *J. Reinf. Plast. Compos.* **2020**, *39*, 119–131. [CrossRef]
19. Yu, K.; Zhu, W.; Ding, Y.; Lu, Z.; Yu, J.; Xiao, J. Micro-structural and mechanical properties of ultra-high performance engineered cementitious composites (UHP-ECC) incorporation of recycled fine powder (RFP). *Cem. Concr. Res.* **2019**, *124*, 105813. [CrossRef]
20. Jiang, H.; Li, F. Effect of recycled fine powder content on mechanical properties of UHPC. *New Build. Mater.* **2020**, *47*, 79–81.
21. Zhang, C.; Wang, Y.; Zhang, X.; Ding, Y.; Xu, P. Mechanical properties and microstructure of basalt fiber-reinforced recycled concrete. *J. Clean. Prod.* **2021**, *278*, 123252. [CrossRef]
22. Liang, C.; Zhang, Y.; Wu, R.; Yang, D.; Ma, Z. The utilization of active recycled powder from various construction wastes in preparing ductile fiber-reinforced cementitious composites: A case study. *Case Stud. Constr. Mater.* **2021**, *15*, e00650. [CrossRef]
23. Li, X.; Lv, X.; Zhou, X.; Meng, W.; Bao, Y. Upcycling of waste concrete in eco-friendly strain-hardening cementitious composites: Mixture design, structural performance, and life-cycle assessment. *J. Clean. Prod.* **2022**, *330*, 129911. [CrossRef]
24. Song, S.; Li, X.; Wang, Z.; Wang, W. Orthogonal experimental and theoretical study on mechanical properties of fiber-reinforced recycled powder concrete. *Case Stud. Constr. Mater.* **2022**, *17*, e01546. [CrossRef]
25. Li, Y.; Zhang, J.; He, Y.; Huang, G.; Li, J.; Niu, Z. A review on durability of basalt fiber reinforced concrete. *Compos. Sci. Technol.* **2022**, *225*, 109519. [CrossRef]
26. Zheng, Y.; Zhang, Y.; Zhuo, J.; Zhang, Y.; Wan, C. A review of the mechanical properties and durability of basalt fiber-reinforced concrete. *Constr. Build. Mater.* **2022**, *359*, 129360. [CrossRef]
27. Wang, J.; Dai, Q.; Si, R.; Guo, S. Investigation of properties and performances of Polyvinyl Alcohol (PVA) fiber-reinforced rubber concrete. *Constr. Build. Mater.* **2018**, *193*, 631–642. [CrossRef]

28. Xu, H.; Shao, Z.; Wang, Z.; Cai, L.; Li, Z.; Jin, H. Experimental study on mechanical properties of fiber reinforced concrete: Effect of cellulose fiber, polyvinyl alcohol fiber and polyolefin fiber. *Constr. Build. Mater.* **2020**, *261*, 120610. [CrossRef]
29. Yu, X.; Li, X.; Ma, R.; Sun, H.; Su, Z. Study on Carbon Emission of Assembled High Ductility Recycled Powder Concrete Structure Based on LCA Theory. *Mater. Rep.* **2024**, *38*, 89–95.
30. Li, X.; Xu, Z.; Bao, Y.; Cong, Z. Post-fire seismic behavior of two-bay two-story frames with high-performance fiber-reinforced cementitious composite joints. *Eng. Struct.* **2019**, *183*, 150–159. [CrossRef]
31. Fan, W.; Su, H.; He, Y.; Sun, W.; Shao, X. Experimental investigation on UHPC-based gravity-type half grouted sleeve connections under tensile and cyclic loadings. *J. Build. Eng.* **2022**, *61*, 105284. [CrossRef]
32. Su, H.; Fan, W.; Wang, H.; Liu, B.; Sun, W.; Shao, X. Direct shear strength of UHPC-based gravity-type grouted sleeve connection members. *J. Build. Eng.* **2023**, *69*, 106266. [CrossRef]
33. Lu, Z.; Wu, B.; Sakata, H.; Huang, J.; Zhang, M. Mechanical performance of prefabricated concrete beam-column joints with double-grouted sleeve connectors: A numerical and theoretical study. *Structures* **2023**, *56*, 104870. [CrossRef]
34. Yang, X.; Jiang, Y.; Lin, F. Experimental study on direct shear resistance of horizontal grouted joints in PC shear walls under compression and in-plane bending moment. *J. Build. Eng.* **2024**, *90*, 109419. [CrossRef]
35. Liu, H.; Chen, J.; Xu, C.; Du, X. Seismic performance of precast column connected with grouted sleeve connectors. *J. Build. Eng.* **2020**, *31*, 101410. [CrossRef]
36. Qiao, D.; Xu, Y.; Zhang, X.; Pang, J.; Liu, K.; Wang, S. Seismic behaviour and size effect of column base joints with inverted exposed grouted sleeves. *J. Build. Eng.* **2022**, *51*, 104333. [CrossRef]
37. Qiao, D.; Sun, H.; Ci, M.; Men, J.; Wang, S. Plastic hinge and damage mechanism of RC assembly column base joint with post pouring area. *Eng. Struct.* **2023**, *294*, 116834. [CrossRef]
38. Wei, Y.; Li, K.; Fan, J.; Li, Y.; Li, S. Seismic performance of RC columns strengthened with HSSSWR meshes reinforced ECC under high axial compression ratio. *J. Build. Eng.* **2023**, *76*, 107350. [CrossRef]
39. Xu, L.; Pan, J.; Cai, J. Seismic performance of precast RC and RC/ECC composite columns with grouted sleeve connections. *Eng. Struct.* **2019**, *188*, 104–110. [CrossRef]
40. Wu, G.; Feng, D. Research progress on fundamental performance of precast concrete frame beam-to-column connections. *J. Build. Struct.* **2018**, *39*, 1–16. [CrossRef]
41. Gao, P.; Deng, Y.; Li, A.; Lu, F. Review on seismic performance of connection joints of prefabricated concrete frame structures. *Ind. Constr.* **2021**, *51*, 171–185+152. [CrossRef]
42. Ding, K.; Ye, Y.; Ma, W. Seismic performance of precast concrete beam-column joint based on the bolt connection. *Eng. Struct.* **2021**, *232*, 111884. [CrossRef]
43. Zhang, Z.; Ding, R.; Nie, X.; Fan, J. Seismic performance of a novel interior precast concrete beam-column joint using ultra-high performance concrete. *Eng. Struct.* **2020**, *222*, 111145. [CrossRef]
44. Xue, W.; Hu, X.; Song, J. Experimental study on seismic behavior of precast concrete beam-column joints using UHPC-based connections. *Structures* **2021**, *34*, 4867–4881. [CrossRef]
45. Huang, W.; Hu, G.; Zhang, J. Experimental study on the seismic performance of new precast concrete beam-column joints with replaceable connection. *Structures* **2022**, *35*, 856–872. [CrossRef]
46. Ye, Y.; Hou, Z.; Qiao, P.; Wang, Z.; Kang, Q. Experimental Study on Seismic Behavior of a new fully precast rocking beam-column joint. *J. Build. Eng.* **2022**, *62*, 105337. [CrossRef]
47. Zhang, J.; Li, C.; Rong, X.; Zhang, X.; Li, Y. Experimental study on the seismic performance of steel–concrete beam–column connections for prefabricated concrete frames. *J. Build. Eng.* **2021**, *43*, 103236. [CrossRef]
48. Zhang, J.; Pei, Z.; Rong, X. Experimental seismic study of an innovative precast steel–concrete composite beam–column joint. *Soil Dyn. Earthq. Eng.* **2022**, *161*, 107420. [CrossRef]
49. Xue, H.; Ashour, A.; Ge, W.; Cao, D.; Sun, C.; Cao, S. Seismic response of prestressed precast reinforced concrete beam-column joints assembled by steel sleeves. *Eng. Struct.* **2023**, *276*, 115328. [CrossRef]
50. Tong, C.; Wu, J.; Zakari, M.; Gao, Y. Hysteretic behavior of a new precast concrete interior beam-to-column joint with a controllable bending moment. *J. Build. Eng.* **2022**, *45*, 103557. [CrossRef]
51. Yang, Y.; Gao, S.; Zheng, Y.; Liu, X.; Zhang, W.; Lin, B. Seismic performance of precast column-beam joint with artificial plastic hinge. *J. Build. Eng.* **2023**, *67*, 105942. [CrossRef]
52. Zhang, X.; Wang, B.; Ju, Y.; Wang, D.; Han, Y.; Song, Y. Seismic performance of precast frame with UHPC composite beams and HSC columns under cyclic loadings. *Eng. Struct.* **2024**, *302*, 117429. [CrossRef]
53. Liu, T.; Zhang, L.; An, X.; Chen, L. Experimental and numerical investigation on collapse behavior of precast reinforced concrete beam-column sub-assemblages with cast-in-place ECC joints. *Case Stud. Constr. Mater.* **2022**, *17*, e01421. [CrossRef]
54. Xiong, X.; Wei, Z.; Zhang, D.; Liu, J.; Xie, Y.; He, L. An Experimental Study on the Seismic Performance of New Precast Prestressed Concrete Exterior Joints Based on UHPC Connection. *Buildings* **2025**, *15*, 729. [CrossRef]

55. Yuan, C.; Cai, J.; Chen, Q.; Liu, X.; Huang, H.; Zuo, Z. Experimental study on seismic behavior of precast recycled fine aggregate concrete beam-column joints with pressed sleeve connections. *J. Build. Eng.* **2022**, *58*, 104988. [CrossRef]
56. Yan, Q.; Chen, T.; Xie, Z. Seismic experimental study on a precast concrete beam-column connection with grout sleeves. *Eng. Struct.* **2018**, *155*, 330–344. [CrossRef]
57. Lin, Y.; Chen, Z.; Guan, D.; Guo, Z. Experimental study on interior precast concrete beam-column connections with UHPC core shells. *Structures* **2021**, *32*, 1103–1114. [CrossRef]
58. Deng, M.; Ma, F.; Song, S.; Lv, H.; Sun, H. Seismic performance of interior precast concrete beam-column connections with highly ductile fiber-reinforced concrete in the critical cast-in-place regions. *Eng. Struct.* **2020**, *210*, 110360. [CrossRef]
59. *JGJ 355-2015*; Ministry of Construction of the People's Republic of China: Technical Specification for Grout Sleeve Splicing of Rebars. China Architecture & Building Press: Beijing, China, 2015.
60. Li, X.; Li, Y.; Yan, M.; Meng, W.; Lu, X.; Chen, K. Cyclic behavior of joints assembled using prefabricated beams and columns with Engineered Cementitious Composite (ECC). *Eng. Struct.* **2021**, *247*, 113115. [CrossRef]
61. *GB 50011-2010*; Ministry of Construction of the People's Republic of China: Code for Seismic Design of Buildings. China Architecture & Building Press: Beijing, China, 2010.
62. Zhu, Z.; Guo, Z.; Liu, J.; Luan, L. Shear bearing performance of precast concrete component interface by bubble film. *China Civ. Eng. J.* **2020**, *53*, 21–27. [CrossRef]
63. *ACI 318-19(22)*; Building Code Requirements for Structural Concrete and Commentary. American Concrete Institute: Farmington Hills, MI, USA, 2022.
64. International Federation for Structural Concrete. *fib Model Code for Concrete Structures 2020: Final Draft*; International Federation for Structural Concrete: Lausanne, Switzerland, 2023.
65. Feng, P.; Qiang, H.; Ye, L. Discussion and definition on yield points of materials, members and structures. *Eng. Mech.* **2017**, *34*, 36–46.
66. Su, J.; Xv, S. Research on cracking behavior of a new type of UHTCC frame beam-column joints. *Ind. Constr.* **2010**, *40*, 99–102. [CrossRef]
67. Xing, G.; Wu, T.; Liu, B. Study on crack resistance of beam-column joints in reinforced concrete frame structures. *Eng. Mech.* **2011**, *28*, 163–169.
68. Hwang, S.; Lee, H. Strength Prediction for Discontinuity Regions by Softened Strut-and-Tie Model. *J. Struct. Eng.* **2002**, *128*, 1519–1526. [CrossRef]
69. Dong, J.; Yang, H.; Zhao, W. Improved diagonal strut model and parameters determination for interior joints in RC frames. *Earthq. Eng. Eng. Dyn.* **2017**, *37*, 155–164.

Disclaimer/Publisher's Note: The statements, opinions and data contained in all publications are solely those of the individual author(s) and contributor(s) and not of MDPI and/or the editor(s). MDPI and/or the editor(s) disclaim responsibility for any injury to people or property resulting from any ideas, methods, instructions or products referred to in the content.